A Structural Model of the Cytochrome c Reductase/Oxidase Supercomplex from Yeast Mitochondria*

Jesco Heinemeyer[‡], Hans-Peter Braun[‡1], Egbert J. Boekema[§2], and Roman Kouřil[§3]

From the [‡]Institute for Plant Genetics, Faculty of Natural Sciences, Universität Hannover, Herrenhäuser Strasse 2,
30419 Hannover, Germany and the [§]Department of Biophysical Chemistry, GBB, University of Groningen,
Nijenborgh 4, 9747 AG Groningen, The Netherlands

Mitochondrial respiratory chain complexes are arranged in supercomplexes within the inner membrane. Interaction of cytochrome c reductase (complex III) and cytochrome c oxidase (complex IV) was investigated in *Saccharomyces cerevisiae*. Projection maps at 15 Å resolution of supercomplexes $III_2 + IV_1$ and $III_2 + IV_2$ were obtained by electron microscopy. Based on a comparison of our maps with atomic x-ray structures for complexes III and IV we present a pseudo-atomic model of their precise interaction. Two complex IV monomers are specifically attached to dimeric complex III with their convex sides. The opposite sides, which represent the complex IV dimer interface in the x-ray structure, are open for complex IV-complex IV interactions. This could lead to oligomerization of $III_2 + IV_2$ supercomplexes, but this was not detected. Instead, binding of cytochrome c to the supercomplexes was revealed. It was calculated that cytochrome c has to move less than 40 Å at the surface of the supercomplex for electron transport between complex III_2 and complex IV. Hence, the prime function of the supercomplex $III_2 + IV_2$ is proposed to be a scaffold for effective electron transport between complexes III and IV.

On a global scale, aerobic respiration provides most of the energy for metabolism and cellular activity. In prokaryotes and mitochondria of eukaryotes it is based on the occurrence of membrane bound oxidoreductase complexes termed complex I (NADH-ubiquinone oxidoreductase), complex II (succinate-ubiquinone oxidoreductase), complex III (ubiquinol-cytochrome c oxidoreductase or cytochrome bc_1 complex), and complex IV (cytochrome c-O_2 oxidoreductase), which together constitute the respiratory chain. The main task of the respiratory chain is to generate the electrochemical proton gradient across the cytoplasmic membrane of prokaryotes or the inner mitochondrial membrane of eukaryotes, which is utilized by complex V (ATP synthase) to synthesize ATP (1, 2).

There is increasing evidence now that three of the respiratory chain complexes and the ATP synthase complex are part of defined supramolecular structures termed respiratory supercomplexes. Mainly due to employment of the detergent digitonin for mild solubilization and Blue native (BN)[4]-PAGE for purification, various supercomplexes were isolated and characterized in several organisms (see Refs. 2– 4 for recent reviews). One main group of supercomplexes consists of combinations of complexes I, III, and IV; one other supercomplex is a homodimer of complex V. At least two forms of yeast III + IV supercomplexes were identified by two-dimensional BN-SDS-PAGE: a $III_2 + IV_1$ and a $III_2 + IV_2$ supercomplex (5, 6). Although structural evidence is so far lacking, inhibitor titration studies, gel filtrations, and immunoprecipitations further support the occurrence of $III_2 + IV_{1-2}$ supercomplexes in yeast (5, 7). In bovine heart mitochondria, up to four copies of complex IV might be bound to dimeric complex III (6). In addition, mammalian $I + III_2 + IV_{1-4}$ supercomplexes were described and named "respirasomes" because they are composed of three of the respiratory chain complexes, which deliver most of the proton motive force to yield ATP (6). Also in bacteria respiratory complexes were reported to form defined supercomplexes (8, 9).

In schematic "text book" representations of the respiratory chain its individual protein complexes are commonly depicted as single copies in a flat membrane, but this is actually an oversimplification of the overall membrane organization. The inner mitochondrial membrane is heavily folded into lamellar or tubular structures termed cristae. In addition, the cristae membrane morphology is dynamic and regulated, at least in part, by proteins that control inter-mitochondrial fission and fusion (10). Electron microscopy three-dimensional reconstructions of quickly frozen mitochondria give the impression of a dynamic interconnected membrane continuum. The lipid to protein ratio within the inner mitochondrial membrane is as low as 1:2–3 (11). There are many indications that this tight packing of proteins in a heavily folded membrane very much restricts the free movement of protein complexes (12). At the same time, the specific way of membrane protein packing most likely influences membrane morphology. Hence, for a closer understanding of respiration, it is necessary to characterize the supramolecular structure of the building blocks of the cristae membranes.

---

[4] The abbreviations used are: BN, Blue native; EM, electron microscopy; Tricine, *N*-[2-hydroxy-1,1-bis(hydroxymethyl)ethyl]glycine; BisTris, 2-[bis(2-hydroxyethyl)amino]-2-(hydroxymethyl)propane-1,3-diol.

Recently, the first projection maps of respiratory supercomplexes were obtained by single particle electron microscopy. Characterization of a I + III$_2$ supercomplex of Arabidopsis revealed lateral association of dimeric complex III to the membrane arm of complex I (13). However, lack of a high-resolution structure of the membrane arm of complex I has so far prevented insight into the precise subunit interactions responsible for formation of this supercomplex. The structure of a dimeric ATP synthase supercomplex was characterized for bovine, Polytomella, and yeast (14–16). Interaction of the monomers takes place between their F$_0$ parts and the long axes of the monomers form angles of up to 90°, resulting in strong local bending of the inner mitochondrial membrane. This bending is believed to be a prerequisite for cristae formation, because yeast mutants lacking dimer-specific ATP synthase subunits lack ATP synthase dimers and at the same time have a flat inner membrane without the characteristic foldings (17, 18). A first projection map of the mammalian I$_1$ + III$_2$ + IV$_1$ supercomplex was also presented recently (19), but lack of detail prevents a consistent modeling of the individual complexes within it. So far, the interaction of complexes III and IV within respiratory supercomplexes is the least understood and therefore was addressed by our current investigation. The advantage of characterizing III–IV supercomplexes is that high resolution structures of the individual complexes III and IV are available.

We have chosen to work on the III$_2$ + IV$_{1-2}$ supercomplexes from the yeast *Saccharomyces cerevisiae* because they were previously shown to be rather stable (5). The tightly associated lipid cardiolipin was found to stabilize this supercomplex (20, 21). Moreover, *S. cerevisiae* does not possess a respiratory chain complex I involved in proton translocation, which reduces the complexity of this supramolecular system. Here, we report projection maps of yeast III$_2$ + IV$_{1-2}$ supercomplexes on the basis of single particle electron microscopy using a set of 86,000 single projections. Various side views and angled side views of particles could be assigned to the supercomplexes. Based on a comparison of our maps for the III$_2$ + IV$_{1-2}$ supercomplexes with the existing atomic x-ray structures for the individual complexes III$_2$ (22) and IV (23), we present a model on their precise interaction. Within the III$_2$ + IV$_2$ supercomplex, complex IV is specifically attached to complex III$_2$ as a monomer on two opposite sides. Complex IV interacts with complex III$_2$ with its convex side which is opposite to the dimer interface within dimeric complex IV as revealed by x-ray crystallography. This supramolecular configuration most likely forms the basis for efficient electron transfer from complex III$_2$ to complex IV by cytochrome *c*, which is partially attached to the III$_2$ + IV$_2$ supercomplex.

EXPERIMENTAL PROCEDURES

Cultivation of S. cerevisiae—*S. cerevisiae* (strain Y187) was cultivated in YPD medium (1 liter of YPD medium contains: yeast extract (10 g), bactopeptone (20 g), D(+)-glucose (20 g)). For mitochondrial isolations, cells were transferred into Lactate medium (2.6 mM glucose, 7.3 mM KH$_2$PO$_4$, 18.7 mM NH$_4$Cl, 4.5 mM CaCl$_2$, 8.6 mM NaCl, 2.9 mM MgCl, 2.2% lactate).

Preparation of Mitochondria—Isolation of yeast mitochondria was based on differential centrifugations and sucrose gradient ultracentrifugation as described by (31). Mitochondria were shock-frozen using liquid nitrogen and stored at −80 °C until use.

Characterization of Mitochondrial Protein Complexes by Blue Native PAGE—Mitochondria from yeast were solubilized by digitonin solution (5% digitonin, 30 mM HEPES, 150 mM potassium acetate, 10% glycerine, pH 7.4), and protein complexes were separated by one-dimensional Blue native PAGE (32, 33). For subunit analysis, gel stripes including the resolved protein complexes were transferred horizontally onto a second gel dimension, which was carried out in the presence of SDS (two-dimensional Blue native/SDS-PAGE). For supercomplex analysis, gel stripes of the Blue native gel were incubated in transfer solution (0.03% dodecyl maltoside, 50 mM Tricine, 15 mM BisTris, 0.02% Coomassie 250G, pH 7.0) and resolved by another Blue native PAGE (6, 34). Gels were either Coomassie-stained (35) or stained by an in-gel activity assay for cytochrome *c* oxidase (36).

Purification of Supercomplexes III$_2$ + IV$_2$—The membrane-bound protein complexes of yeast were solubilized using digitonin solution (5% digitonin, 30 mM HEPES, 150 mM potassium acetate, 10% glycerol, pH 7.4) and separated by sucrose gradient ultracentrifugation (gradients of 0.3–1.5 M sucrose, 15 mM Tris base, pH 7.0, 20 mM KCl, 0.2% digitonin; centrifugation for 17 h at 150,000 × *g* at 4 °C). Afterward, the gradients were fractionated and the protein complex compositions of the fractions analyzed by one-dimensional Blue native PAGE.

Electron Microscopy—Selected fractions of the gradients including supercomplexes of complex III and complex IV were directly used for electron microscopy and single particle analyses. Samples of purified complexes were negatively stained by using the droplet method with 2% uranyl acetate on glow-discharged, carbon-coated copper grids. Electron microscopy was performed on a CM120 electron microscope (FEI, Eindhoven, The Netherlands) operated at 120 kV. Images were recorded under low dose conditions (a total dose ~25 e$^-$/Å^2) with a 4000 SP 4K slow-scan CCD camera (Gatan, Pleasanton, CA) at −340 nm defocus and at the final magnification of 80,000 at the level of the CCD camera with GRACE software for semi-automated specimen selection and data acquisition (37). The pixel size (after binning the images) was 3.75 Å at the specimen level. In total, about 4.300 images were recorded and over 86,000 single particle projections were selected for image analysis. A major part of the projections was selected using Boxer, a graphical program for semiautomatic particle selection from EMAN software package (38). Single-particle analysis was performed with the Groningen Image Processing (GRIP) software package on a PC cluster. Selected single-particle projections were aligned by multireference and reference-free alignment procedures (37, 39). Particles were then subjected to multivariate statistical analysis followed by hierarchical classification (39). From the whole data set, almost 85% of single particles were assigned to specific supercomplexes, of which the III$_2$ + IV$_2$ and III$_2$ + IV$_1$ supercomplexes were present in almost equal amount (about 44 and 41%, respectively). Final two-dimensional projection maps of different angular views of the III$_2$ + IV$_2$ and III$_2$ + IV$_1$ supercomplexes were calculated from the best resolved classes, which represented about 20% of whole data set. The remaining
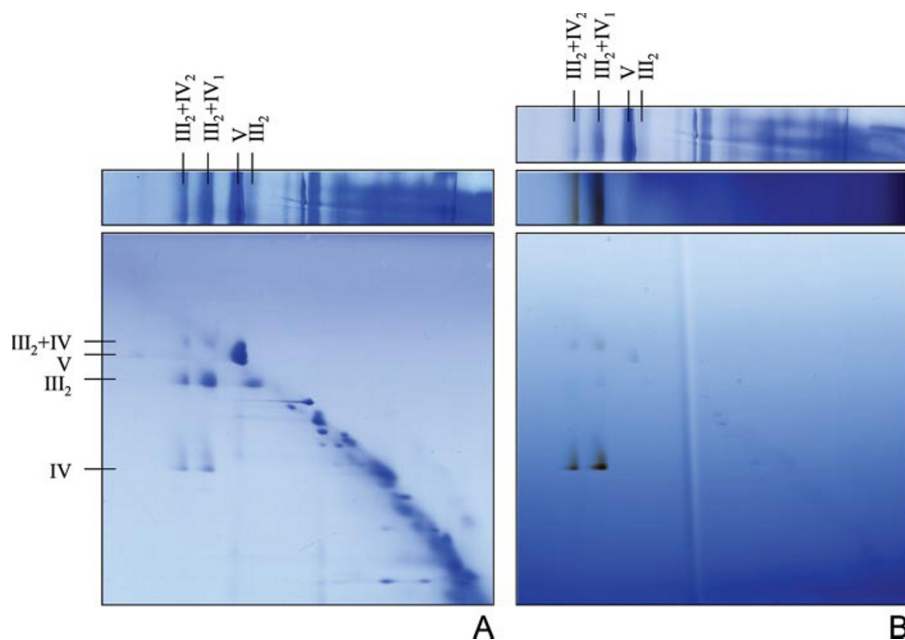
FIGURE 1. **Characterization of the III$_2$ + IV$_2$ and III$_2$ + IV$_1$ supercomplexes.** Mitochondrial proteins from yeast (1 mg) were separated by two-dimensional Blue native/Blue native PAGE. Gels were stained by Coomassie Blue (*A*) or by an in-gel activity assay for complex IV (*B*). Under the applied conditions, the supercomplexes are dissected into dimeric complex III and monomeric complex IV. Monomeric complex IV was absent on the first gel dimension, indicating that it is exclusively present as part of the supercomplexes.
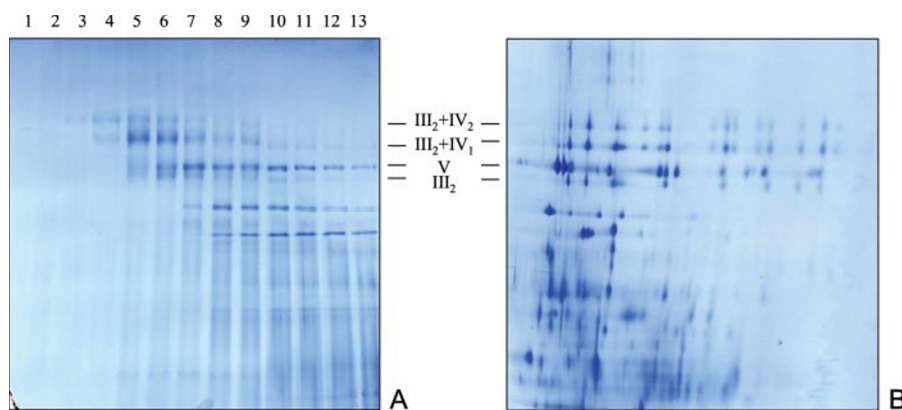

FIGURE 2. **Purification of the III$_2$ + IV$_2$ and III$_2$ + IV$_1$ supercomplexes by sucrose gradient ultracentrifugation.** Mitochondrial membrane proteins from yeast were solubilized by digitonin (5 g detergent per g protein) and resolved by ultracentrifugation as described under "Experimental Procedures." The sucrose gradient was fractionated into 13 fractions from bottom to top. All fractions were analyzed by one-dimensional Blue native-PAGE (*A*) to monitor their protein complex content. Protein complexes were identified by a parallel two-dimensional Blue native-SDS-PAGE of a mitochondrial fraction of yeast (*B*). Fractions 4 and 5 of the sucrose gradient contain the III$_2$ + IV$_2$ and III$_2$ + IV$_1$ supercomplexes and were used for EM and single particle analysis. *III$_2$*: dimeric complex III; *V*, monomeric complex V; *III$_2$ + IV$_1$*, supercomplex composed of dimeric complex III and monomeric complex IV; *III$_2$ + IV$_2$*, supercomplex composed of dimeric complex III and two copies of monomeric complex IV.

the III$_2$ + IV$_2$ and III$_2$ + IV$_1$ supercomplexes were constructed manually using Swiss Protein Data Bank viewer (41). First, a starting model of the most symmetrical view of the III$_2$ + IV$_2$ supercomplex (Fig. 5*A*) was constructed. Importantly, a contact (or a distance) between the complexes III and IV in the starting model was such that there were no clashes detected between transmembrane helices of the complexes III and IV within 2 Å. Afterward, the model of the III$_2$ + IV$_2$ supercomplex was closely fitted into the EM averaged projection. Subsequently, the tilted views of the III$_2$ + IV$_2$ and III$_2$ + IV$_1$ supercomplexes (coordinates of one complex IV monomer were deleted from the Protein Data Bank file) were generated solely by a rotation of the whole starting model and manually fitted into the tilted EM projections. If structural inconsistencies were found, the starting model was modified. The position of complex IV with respect to complex III was repeatedly changed by a rotational increment of about 20° followed by fine shifts and rotations until all generated models of the III$_2$ + IV$_2$ and III$_2$ + IV$_1$ supercomplexes closely matched the EM maps. Different views of the III$_2$ + IV$_2$ and III$_2$ + IV$_1$ supercomplexes were finally displayed using PyMOL software (42). Truncated versions and two-dimensional projection maps of the generated models for the III$_2$ + IV$_2$ and III$_2$ + IV$_1$ supercomplexes at 15 Å resolution were generated using routines from the EMAN package (38).

RESULTS

All Complex IV Is Bound to a Dimeric Complex III$_2$ Scaffold—The presence and composition of complex III$_2$ + IV$_{1-2}$ supercomplexes after membrane solubilization with the detergent digitonin was first explored by BN-PAGE (Fig. 1). Using one-dimensional native gels, III$_2$ + IV$_{1-2}$ supercomplexes are visible at ~650 and ~850 kDa in accordance with previous investigations (6). A two-dimensional BN/BN-PAGE system, which is carried out in the presence of digitonin for the first gel dimension and in the presence of dodecylmaltosid for the second, was employed to investigate the protein complex composition of the two supercomplexes. Under the conditions applied, both supercomplexes are dissected into monomeric complex IV (~200 kDa) and dimeric

classes represented the same views of supercomplexes, however, with less resolved features. Resolution was measured using Fourier-ring correlation and the 3 σ criterion (40).

X-ray structures of the yeast cytochrome *c* reductase (22) and the bovine heart cytochrome *c* oxidase (23) were used for generating the pseudo-atomic model of the III$_2$ + IV$_2$ and III$_2$ + IV$_1$ supercomplexes (the Protein Data Bank accession numbers 1KB9 and 1OCC, respectively). Mammalian subunits Cox VIIb and Cox VIII, which are not present in the yeast cytochorme *c* oxidase, were removed from the x-ray data file. Atomic coordinates of cytochrome *c* were obtained from (22) (the Protein Data Bank accession number 1KYO). Pseudo-atomic models of
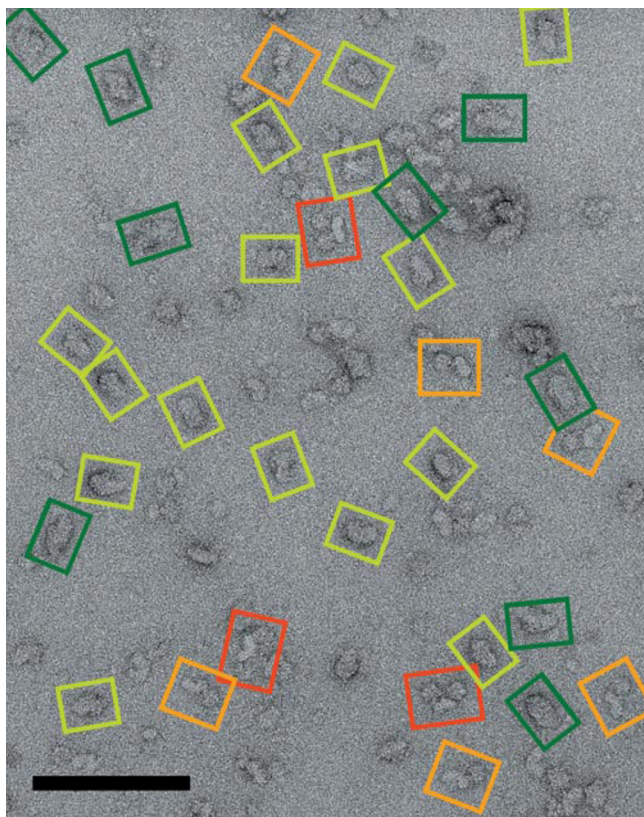
FIGURE 3. **Part of an electron micrograph of membrane proteins from the fraction 5 obtained by sucrose gradient centrifugation.** *Dark green* and *light green boxes* indicate $III_2 + IV_2$ and $III_2 + IV_1$ supercomplexes, respectively. Intact complex V_2 and fragments of complex V_2 are indicated by *red* and *orange boxes*, respectively. The *space bar* is 100 nm.
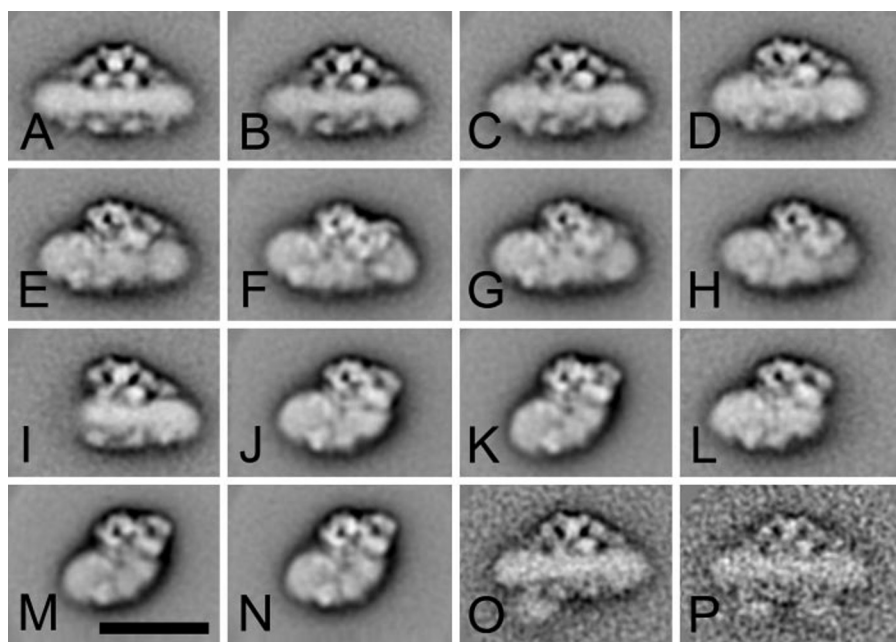
complex III ($\sim$450 kDa) as reported previously (6). The ratio of complex IV to complex III_2 clearly differs within the supercomplexes, with complex IV being relatively less abundant within the smaller supercomplex. The two supercomplexes were interpreted as supercomplex $III_2 + IV_1$ (650 kDa) and $III_2 + IV_2$ (850 kDa). In-gel complex IV activity staining reveals that complex IV of the supercomplex is active (Fig. 1*B*). Furthermore, activity staining reveals that all complex IV is present within the two supercomplexes. No free monomeric ($\sim$200 kDa) or dimeric ($\sim$400 kDa) forms of complex IV were detected upon detergent solubilization, indicating that complex IV is completely bound to dimeric complex III within the yeast mitochondrial membrane.

Multiple Projection Views of the $III_2 + IV_2$ and $III_2 + IV_1$ Supercomplexes—To obtain $III_2 + IV_{1-2}$ supercomplexes free of Coomassie Blue, which might alter supercomplex structure due to the introduction of negative charge, proteins of digitonin-treated mitochondrial fractions were resolved by sucrose gradient ultracentrifugation (Fig. 2*A*). The protein complex content of the fractions of the gradient was subsequently analyzed by one-dimensional BN-PAGE. Sucrose gradient fractions 4 and 5 were found to include the 650- and 850-kDa supercomplexes in the purest form. Separation of the subunits of the two supercomplexes by two-dimensional BN-SDS-PAGE revealed the known subunits of the complexes III and IV, which previously were identified by cyclic Edman degradation (6) (Fig. 2*B*).

Electron microscopy of negatively stained specimens of the sucrose gradient fractions 4 and 5 revealed the presence of complexes with variable size and shape, which could potentially represent views of the $III_2 + IV_1$ and $III_2 + IV_2$ supercomplexes with varying orientations on the carbon support film (Fig. 3).

From about 4300 electron micrographs, all plausible projections of the $III_2 + IV_2$ and $III_2 + IV_1$ supercomplexes were selected and a data set of over 86,000 single particle projections was subjected to image analysis. The analysis revealed that fraction 4 was almost free of other supercomplexes, whereas fraction 5 (Fig. 3) also contained dimeric ATP synthase particles, which have a very different shape. (An analysis of 20,000 supercomplex V_2 projections is presented in (16)). Fig. 4 shows the gallery of the best resolved two-dimensional projection maps obtained by statistical analysis and classification. Fig. 4*A* represents the most symmetrical view of the supercomplex. As the central part of the supercomplex exhibits the characteristic shape and features of the x-ray structure of dimeric complex III and the dimensions of the two additional densities are similar to the dimensions of the x-ray model of complex IV, the

FIGURE 4. **Single particle electron microscopy of the $III_2 + IV_2$ and $III_2 + IV_1$ supercomplexes purified from the yeast *S. cerevisiae*.** Projection maps (*A*–*H*) represent class sums of 832 (*A*), 768 (*B*), 962 (*C*), 743 (*D*), 1000 (*E*), 1024 (*F*), 2440 (*G*), and 1648 (*H*) aligned projections of the $III_2 + IV_2$ supercomplex with different orientations on the support carbon film, respectively. *I*–*N* represent class sums of 768 (*I*), 2048 (*J*), 2048 (*K*), 717 (*L*), 1765 (*M*), and 2048 (*N*) aligned projections of the $III_2 + IV_1$ supercomplex. Projection maps (*O*, *P*) represent class sums of 75 and 16 aligned particles of the $III_2 + IV_2$ supercomplex with either one or two additional densities in the lower part of the projections, respectively. The *scale bar* equals 20 nm.
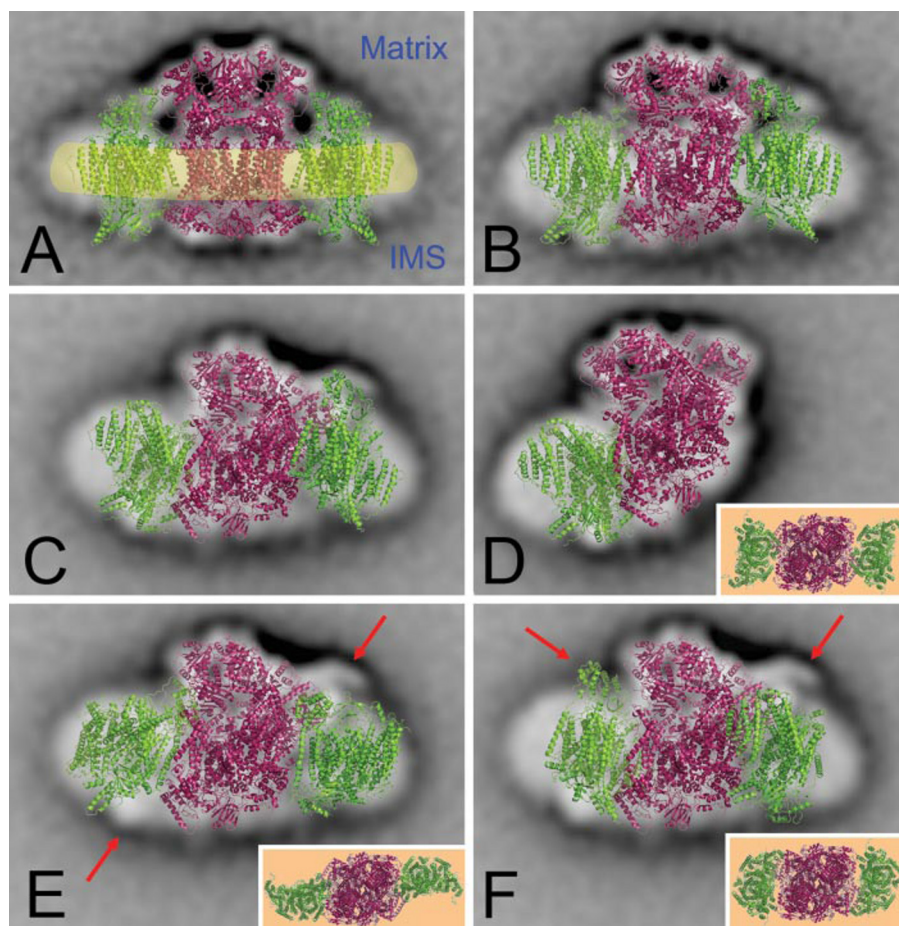
FIGURE 5. **Fitting of atomic structures of the yeast cytochrome bc_1 complex (*red*) and the bovine heart cytochrome *c* oxidase or complex IV (*green*) into selected EM projection maps for assignment of the arrangement of the $III_2 + IV_2$ and $III_2 + IV_1$ supercomplexes.** One common pseudo-atomic model was constructed (presented in the membrane plane in the *inset* of *D*) and used for generating different overlays closely matching the $III_2 + IV_2$ (*A–C*) and $III_2 + IV_1$ (*D*) supercomplex maps, respectively. The membrane is depicted in *yellow* in *A*. The extended length of the $III_2 + IV_2$ average structures obtained by EM compared with the pseudo-atomic structure most likely is due to the presence of both detergent and membrane lipids bound to the membrane-spanning regions of the supercomplex. *E* and *F*, examples of alternative fitting models in which the position of the complex IV monomers was changed by a 90 and 180° rotation in the membrane plane (see *insets* of *E* and *F*). *Red arrows* indicate the most pronounced mismatches between these alternative models and corresponding EM maps.

averaged projection in Fig. 4*A* could be unambiguously assigned to the side view of the $III_2 + IV_2$ supercomplex (see below). Fig. 4, *B–H*, represents averaged projections of slightly tilted views of the $III_2 + IV_2$ supercomplex. In addition to the $III_2 + IV_2$ supercomplex, different projections of a smaller supercomplex containing only one copy of complex IV were also found (Fig. 4, *I–N*). Interestingly, extensive analysis of the whole data set revealed about 100 particles which show characteristic features of the $III_2 + IV_2$ supercomplex, and one or two additional densities on the intermembrane-space-exposed side of the supercomplex (Fig. 4, *O* and *P*, respectively). This additional density is attached to complex III_2 at the position of the mobile electron transporter cytochrome *c*, as present in the x-ray structure of the complex III_2+cytochrome *c* particle of yeast (22).

Fitting of X-ray Models of Complexes III and IV to Averaged EM Projections—To interpret the EM projection maps of the $III_2 + IV_2$ and $III_2 + IV_1$ supercomplexes, they were compared with atomic x-ray structures of yeast complex III (22) and

bovine heart complex IV (23), as the x-ray structure of the yeast complex IV has not been solved yet. Although the bovine heart complex IV contains two additional subunits (Cox7b and Cox8) compared with yeast complex IV, the overall structure of the yeast complex IV can be considered to be similar to its mammalian counterpart (24). First, the largest core subunits Cox1, Cox2, and Cox3, which represent the major part and active core of the complex, are highly conserved in eukaryotes. Second, the other subunits are less conserved, however, they are smaller than the core subunits and several of them, including Cox7b and Cox8, are represented merely by a single transmembrane helix. As the resolution in the best EM projections was about 15 Å, we assume that the x-ray structure of the bovine complex with excluded Cox7b and Cox8 subunits can be substituted for the structure of the yeast complex IV.

Unambiguous assignment of the complex III dimer to the central part of the supercomplex is facilitated by the characteristic shape and well resolved features of the almost 100-kDa membrane-protruding core 1 and 2 subunit moieties (Fig. 4). This implies that complex IV is peripherally located. One copy is flanking each side of the complex III dimer in the $III_2 + IV_2$ supercomplex, which means that complex IV is not present as a dimer in the supercomplex, although it is present as a dimer in the crystals used for structure determination (23). It is also obvious that one copy of complex IV is lacking in a substantial number of particles (Fig. 4, *I–N*). Determination of the exact orientation of complex IV was more difficult due to the presence of a detergent shell and less resolved features of the complex IV in the projection maps. The availability of various angular projections of the $III_2 + IV_2$ and $III_2 + IV_1$ supercomplexes turned out to be crucial for an unambiguous assignment of the complex IV orientation and its interaction with the complex III_2 within the supercomplex. A pseudo-atomic model of the whole supercomplex was constructed (see "Experimental Procedures") and compared with different angular projection maps of the $III_2 + IV_2$ and $III_2 + IV_1$ supercomplexes (Fig. 4, *A*, *D*, *F*, and *J*).

Fig. 5*A* shows the side view of the pseudo-atomic model, which unambiguously matches the EM averaged projection of the $III_2 + IV_2$ supercomplex presented in Fig. 4*A*. In the model, membrane-protruding parts of both complex III_2 and complex

IV closely fit the densities of our EM projection. Furthermore, the stain accumulated areas in the EM projection correspond to low density areas in the model of the supercomplex. The extended width of the EM projection at the membrane plane compared with the atomic model can be explained by the presence of a negative stain-excluding detergent shell. However, molecular flattening of a partially stained membrane part upon air drying cannot be fully excluded and also could explain the observed lateral extensions (43). Fig. 5, *B* and *C*, show that computer generated tilted views of the atomic model closely match the tilted EM projections of the $III_2 + IV_2$ supercomplex. Finally, Fig. 5*D* shows a close matching of the atomic model of the $III_2 + IV_1$ supercomplex over the averaged EM projection. Importantly, a close match of the complex IV in our pseudo-atomic model with angular projection maps of the $III_2 + IV_2$ and $III_2 + IV_1$ supercomplexes (Fig. 4, *F* and *J*) was exclusively obtained when the complex IV faces the complex III_2 with its convex side which is the opposite of the dimer interface in the x-ray structure of dimeric complex IV (Fig. 5*D*, *inset*). Any other orientation of the complex IV with respect to the complex III_2 did not lead to a consistent fitting into our EM projection maps; there was always at least one map, which did not match with such models. This is exemplified by Fig. 5, *E* and *F*, which show two extreme positions of complex IV that differ by 90 and 180°. These models, depicted as *insets* of Fig. 5, *E* and *F*, clearly do not lead to a close match with one specific tilted view of the $III_2 + IV_2$ supercomplex. In particular, the matrix exposed part of the complex IV does not fit with resolved EM densities of the $III_2 + IV_2$ supercomplex (see *red arrows* in Fig. 5, *E* and *F*), which rules out these hypothetical associations of the complex IV to the complex III_2.

Once pseudo-atomic models of the $III_2 + IV_2$ and $III_2 + IV_1$ were constructed, truncated two-dimensional projection maps of x-ray models could be generated and compared with EM projection maps (Fig. 6). Visual comparison indicates that the overall shape of generated two-dimensional projection maps is similar to the shape of supercomplexes revealed by single particle EM. Particularly, characteristic features of the complex III_2 revealed in the EM projections are well recognizable in generated two-dimensional projection maps too. Stain accumulated areas in the EM projections of the complex III_2 correspond well to the low density areas in the generated two-dimensional projection maps. Although the presence of detergent reduces resolution of the complex IV in EM projection maps, it is evident that the overall shape and the position of the complex IV in the generated two-dimensional projections are consistent with experimental data.

DISCUSSION

Structural characterization of the individual respiratory chain complexes and their interactions within the inner mitochondrial membrane are of prime importance for a better understanding of oxidative phosphorylation, the major function of mitochondria. Furthermore, recent investigations indicate that respiratory supercomplexes are the building blocks of the higher order structure of the mitochondrial membranes. This publication reports a structural characterization of the yeast $III_2 + IV_{1-2}$ supercomplexes by single particle electron
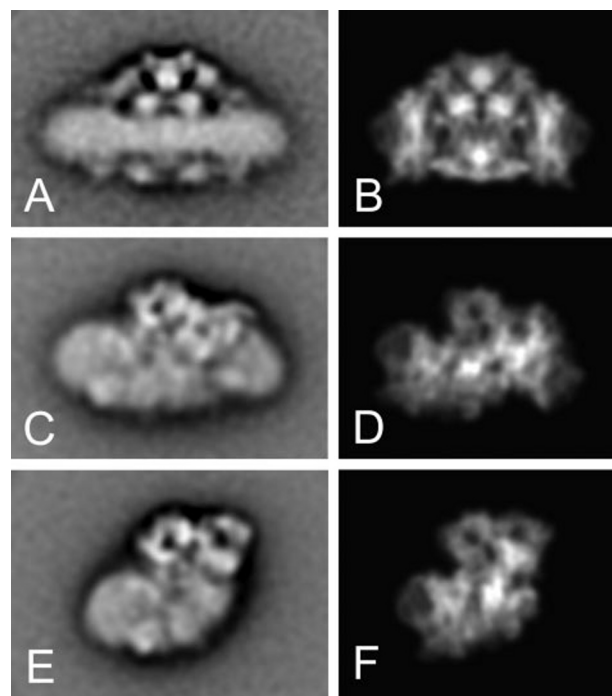

FIGURE 6. **Comparison of selected EM projection maps of the $III_2 + IV_2$ (*A, C*) and $III_2 + IV_1$ (*E*) supercomplexes with two-dimensional projection maps generated from the proposed pseudo-atomic models of the $III_2 + IV_2$ (*B, D*) and $III_2 + IV_1$ (*F*) supercomplexes at 15 Å resolution.**

microscopy. In principle, the optimal way to do such a structural investigation is to perform a three-dimensional reconstruction from low contrast ice-embedded unstained samples. However, this is often not feasible because such labile supercomplexes cannot be purified to homogeneity at a high concentration and need to be kept in the presence of detergent to maintain covering of their hydrophobic surface parts. A good compromise is to perform EM investigations in a classical high-contrast medium, such as the negative stain uranyl acetate. Analysis of a large data set of over 86,000 particle projections revealed various angular two-dimensional projection maps of the $III_2 + IV_2$ and $III_2 + IV_1$ supercomplexes at 15 Å resolution in the best classes (Fig. 4), which enabled us to compare our two-dimensional projections with x-ray structures of the yeast complex III and bovine heart complex IV and construct a pseudo-atomic model of the $III_2 + IV_2$ supercomplex (Fig. 5). Given the resolution of 15 Å for the projection maps, the estimated precision of the fitting is at best at 10 Å, which means that it is not possible to indicate particular amino acid residues involved in the interaction, but valid to indicate subunit interactions that are within 20 Å range of each other. Resolution of different angular EM projections of the $III_2 + IV_2$ and $III_2 + IV_1$ supercomplexes was found to be essential for unambiguous determination of the complex IV position and orientation in a pseudo-atomic model. On the basis of simulations, we can conclude that complex IV has to interact with the complex III through its convex side, which is the opposite side of the complex IV dimer interface in the x-ray structure (Fig. 7*B*). Any other orientation of the complex IV within the pseudo-atomic model did not lead to a successful simulation of all resolved EM maps of the $III_2 + IV_2$ and $III_2 + IV_1$ supercomplexes (Fig. 5). Generation of trun-
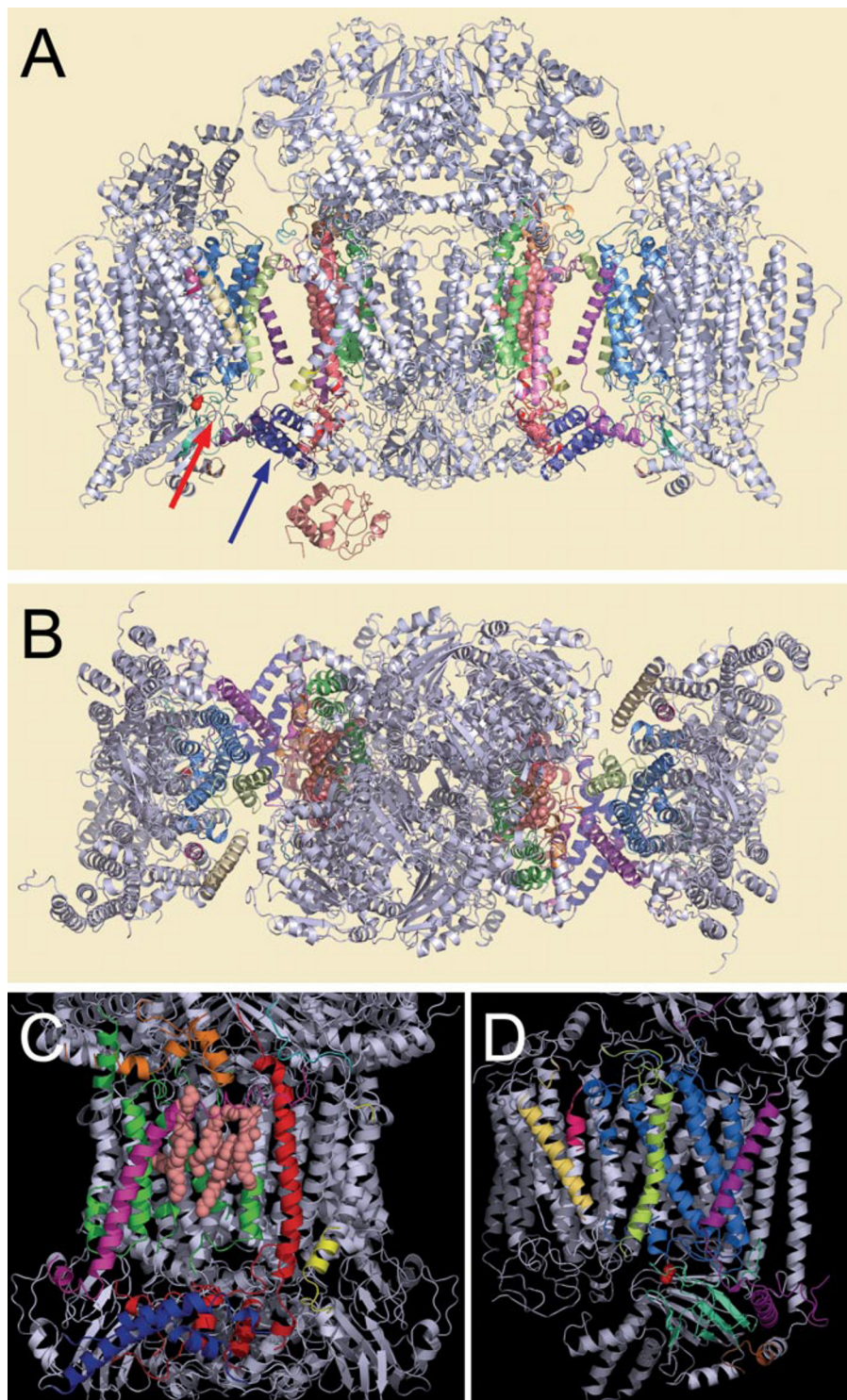
FIGURE 7. **Pseudo-atomic model of the III$_2$ + IV$_2$ supercomplex with attached cytochrome *c*, showing the interactions between complexes III and IV.** *A*, side view of the III$_2$ + IV$_2$ supercomplex with cytochrome *c*, bound to complex IV. *Blue* and *red arrows* indicate the hinge protein (QCR6) of complex III and the cytochrome *c* binding pocket of complex IV, respectively. The first electron acceptors of complex IV, Cu$_A$ atoms, are depicted as a *red spheres*. *B*, top view of the III$_2$ + IV$_2$ supercomplex from the matrix side of the membrane. *C* and *D*, detailed view on interaction sides of complex III or complex IV showing subunits involved in interaction with either complex IV or complex III, respectively. Helices and loops of the complex III and IV, which are within 20 Å distance of each other, are highlighted in colors: *green*, cytochrome *b*; *red*, cytochrome *c$_1$*; *cyan*, RIP1; *blue*, QCR6 (hinge protein); *orange*, subunit QCR7; light magenta, subunit QCR8; *yellow*, QCR9; *salmon*, cardiolipin and phosphatidyl ethanolamine molecules of the complex III and subunits Cox I (*navy blue*), Cox II (*green cyan*), Cox III (*hot pink*), Cox IV (*purple*), Cox VIc (*brown*), Cox VIIa (*yellow orange*), and Cox VIIc (*green yellow*) of the complex IV, respectively.

cated two-dimensional projection maps of x-ray models revealed similar density profiles observed in EM projection maps (Fig. 6), which further supports the correctness of our proposed model. Cox I, Cox II, Cox III, Cox IV, Cox VIc, Cox VIIa, and Cox VIIc subunits of complex IV were found to be involved in varying degrees in the interaction with complex III (Fig. 7D). Although involvement of Cox I, Cox II, and Cox III in interaction with complex III has been predicted previously by deletion studies, the exact orientation of the complex IV relative to complex III remained unclear (21, 25). It is important to realize that due to a different nomenclature Cox IV, CoxVIc, Cox VIIa, and Cox VIIc in mammals refer to CoxV, CoxVIIa, Cox VII, and Cox VIII in yeast, respectively. On the complex III$_2$ side, cytochrome *b*, cytochrome *c$_1$*, QCR6 (hinge protein), QCR7, QCR8, QCR9, cardiolipin, and phosphatidylethanolamine molecules were identified at the complex III$_2$-IV interface (Fig. 7C). Although cytochrome *b* and cytochrome *c$_1$* were considered as the most likely candidates for a direct link between complexes III and IV (5, 25, 21), direct evidence supporting their gluing function was missing so far. Similarly, there was no structural evidence proving a close position of QCR6, QCR7, QCR8, and QCR9 to the complex III–IV interaction side. Localization of cardiolipin at the complex III–IV interaction interface further supports its essential role in formation of yeast supercomplexes, as was recently reported (20, 21). In addition, the fitting of the complexes within the supercomplex was generally close for all parts, except for the Rieske FeS subunit of complex III. However, this subunit is known to undergo conformational changes of about 20 Å during catalysis (26).

Previous investigations have indicated that purified bovine heart complex IV is in either a monomeric or a dimeric state, depending on the presence of lipids and the type of

detergent used for solubilization. In the three-dimensional crystals, which were used for x-ray crystallography, complex IV is dimeric (27). However, the nature and the physiological significance of the dimer is still a matter of debate. Intermonomer interactions are strong enough to prevent the dimer from spontaneous dissociation and thus the dimeric state could be dominant in the membrane (27). Surprisingly, BN-PAGE does not reveal complex IV forms outside the $III_2 + IV_{1-2}$ supercomplexes, neither in monomeric nor in dimeric form (Fig. 1 and 2). The supercomplex-bound form of complex IV is always a monomer. However, since the proposed interface important for complex IV dimerization is on the opposite side of the complex IV-complex III_2 interface, the $III_2 + IV_{1-2}$ supercomplex structures do not exclude the possibility of complex IV-complex IV interactions in *in vivo* conditions. Occurrence of these interactions would allow oligomerization of $III_2 + IV_2$ supercomplexes into long "string"-like structures, which previously were proposed for mammalian mitochondria (28). However, we found no direct evidence for the presence of such strings in yeast, *e.g.* particles of dimeric complex IV bound to dimeric complex III. In contrast a couple of dozen $III_2 + IV_2$ supercomplex particles were found, which include 1–2 copies of cytochrome *c* (see below). Therefore, complex IV-complex IV binding, if existing at all, seems to be at least weaker than binding of cytochrome *c* to the $III_2 + IV_2$ supercomplex in yeast. This does not necessarily imply that mitochondria from other organisms need to have the same type of membrane complex organization. In bovine mitochondria, the ratio of complex IV to III is two times higher than in yeast (2). Another difference is that complex I, which is absent in *S. cerevisiae*, is expected to interact with the $III_2 + IV_{1-2}$ supercomplexes in other organisms.

Single particle analysis indicated small numbers of an additional protein binding at the interface of complexes III and IV at one or two positions (Fig. 4, *O* and *P*). The fuzzy appearance in the average map of Fig. 4*O* indicates small flexibilities upon binding which results in a smeared-out projection density. It is interpreted as cytochrome *c*, because this protein is known to bind at this side of complexes III and IV. It was shown in yeast that cytochrome *c* is protected from degradation by interaction with both complex III and complex IV (29). We can suggest that some of the 75 particles, which were used for the class sum shown in Fig. 4*O*, represent situations in which cytochrome *c* is in an intermediate position between the two binding sites. Subunits like, *e.g.* the hinge protein of complex III, which was found to be essential for a binding of cytochrome *c* to complex III (44), can be important for transfer and channeling of cytochrome *c* from complex III to complex IV. The short distance between the cytochrome *c* binding sites on complexes III and IV can facilitate electron transfer mediated by cytochrome *c* within the supercomplex (Fig. 7*A*). Previous x-ray data and computing simulations indicated that the distance between the heme iron of cytochrome *c* and either the heme iron of the cytochrome c_1 (electron donor of the complex III) or the Cu_A atom (the first electron acceptor of the complex IV), is about 18 Å, which allows a direct electron transfer between appropriate redox pairs and cytochrome *c* (22, 30). Taking the above mentioned distances into account, our pseudo-atomic model of the supercomplex shows that cytochrome *c* has to move and rotate

within 40 Å to be able to mediate electron transfer between the complexes III and IV.

In conclusion, our data indicate one single and specific type of interaction between complexes III and IV in yeast but no higher ordering of these supercomplexes into strings or other types of oligomers. This is in contrast to the V_2 supercomplex, which appears to form a defined type of oligomer in which dimeric ATP synthase supercomplexes associate in long rows (3, 15, 16). There is increasing evidence that this oligomer has a special function of inducing local membrane curvature, because the ATP synthase monomers within the oligomers make angles of 35–90° with their neighbors across and along the direction of the oligomers. In contrast the $III_2 + IV_2$ supercomplex is a flat structure embedded within the membrane plane. Because the membrane is strongly negative stain-excluding, the overall position of the lipid membrane can be fitted as indicated in Fig. 5*A*. The fitting is in agreement with the position of the membrane-spanning helices according to the atomic models (22, 23). The fitting shows that the membrane could be slightly curved (up to 4°), but certainly not very much kinked as it was found for the ATP synthase dimer (16). Hence we conclude that it does not have a defined role in folding of the inner mitochondrial membrane. However, formation of the $III_2 + IV_2$ supercomplex most likely has important physiological implications, because electron transport between complex III_2 and complex IV can be realized by a simple ping-pong movement of cytochrome *c* between the these two complexes. Indeed the cytochrome *c* binding sites on complex III_2 and complex IV within the supercomplex are in very close proximity. It was previously shown by inhibitor titration experiments that cytochrome *c* does not exhibit pool behavior in yeast and that the whole respiratory chain of yeast behaves like a single functional unit (7). Our structural data suggest that the $III_2 + IV_2$ supercomplex forms the core of this functional unit in yeast and probably in many other species.

REFERENCES

1. Saraste, M. (1999) *Science* **283,** 1488–1493
2. Schägger, H. (2002) *Biochim. Biophys. Acta* **1555,** 154–159
3. Dudkina, N. V., Heinemeyer, J., Sunderhaus, S., Boekema, E. J., and Braun, H. P. (2006a) *Trends Plant Sci.* **11,** 232–240
4. Heinemeyer, J., Dudkina, N. V., Boekema, E. J., and Braun, H. P. (2007) in *Plant Mitochondria, Annual Plant Reviews Series* (Logan, D. C., ed) Blackwell Publishing, Oxford, UK, in press
5. Cruciat, C. M., Brunner, S., Baumann, F., Neupert, W., and Stuart, R. A. (2000) *J. Biol. Chem.* **275,** 18093–18098
6. Schägger, H., and Pfeiffer, K. (2000) *EMBO J.* **19,** 1777–1783
7. Boumans, H., Grivell, L. A., and Berden, J. A. (1998) *J. Biol. Chem.* **273,** 4872–4877
8. Berry, E. A., and Trumpower, B. L. (1985) *J. Biol. Chem.* **260,** 2458–2467
9. Stroh, A., Anderka, O., Pfeiffer, K., Yagi, T., Finel, M., Ludwig, B., and Schägger, H. (2004) *J. Biol. Chem.* **279,** 5000–5007
10. Mannella, C. A. (2006) *Biochim. Biophys. Acta* **1763,** 542–548
11. Schwerzmann, K., Cruz-Orive, L. M., Eggman, R., Sänger, A., and Weibel, E. R. (1986) *J. Cell Biol.* **102,** 97–103
12. Allen, R. D., Schroeder, C. C., and Fok, A. K. (1989) *J. Cell Biol.* **108,** 2233–2240

13. Dudkina, N. V., Eubel, H., Keegstra, W., Boekema, E. J., and Braun, H. P. (2005a) *Proc. Natl. Acad. Sci. U. S. A.* **102,** 3225–3229

14. Minauro-Sanmiguel, F., Wilkens, S., and Garcia, J. J. (2005) *Proc. Natl. Acad. Sci. U. S. A.* **102,** 12356–12358

15. Dudkina, N. V., Heinemeyer, J., Keegstra, W., Boekema, E. J., and Braun, H. P. (2005b) *FEBS Lett.* **579,** 5769–5772

16. Dudkina, N. V., Sunderhaus, S., Braun, H. P., and Boekema, E. J. (2006b) *FEBS Lett.* **580,** 3427–3432

17. Paumard, P., Vaillier, J., Coulary, B., Schaeffer, J., Soubannier, V., Mueller, D. M., Brethes, D., di Rago, J. P., and Velours, J. (2002) *EMBO J.* **2,** 221–230

18. Giraud, M. F., Paumard, P., Soubannier, V., Vaillier, J., Arselin, G., Salin, B., Schaeffer, J., Brèthes, D., di Rago, P., and Velours, J. (2002) *Biochim. Biophys. Acta* **1555,** 174–180

19. Schäfer, E., Seelert, H., Reifschneider, N., Krause, F., Dencher, N. A., and Vonck, J. (2006) *J. Biol. Chem.* **281,** 15370–15375

20. Zhang, M., Mileykovskaya, E., and Dowhan, W. (2002) *J. Biol. Chem.* **277,** 43553–43556

21. Pfeiffer, K., Gohil, V., Stuart, R. A., Hunte, C., Brandt, U., Greenberg, M. L., and Schägger, H. (2003) *J. Biol. Chem.* **278,** 52873–52880

22. Lange, C., and Hunte, C. (2002) *Proc. Natl. Acad. Sci. U. S. A.* **99,** 2800–2805

23. Tsukihara, T., Aoyama, H., Yamashita, E., Tomizaki, T., Yamaguchi, H., Shinzawa-Itoh, K., Nakashima, R., Yaono, R., and Yoshikawa, S. (1996) *Science* **272,** 1136–1144

24. Khalimonchuk, O., and Rödel, G. (2005) *Mitochondrion* **5,** 363–388

25. Schägger, H. (2001) *IUBMB Life* **52,** 119–128

26. Zhang, Z., Huang, L., Shulmeister, V. M., Chi, Y. I., Kim, K. K., Hung, L. W., Crofts, A. R., Berry, E. A., and Kim, S. H. (1998) *Nature* **392,** 677–684

27. Lee, S. J., Yamashita, E., Abe, T., Fukumoto, Y., Tsukihara, T., Shinzawa-Itoh, K., Ueda, H., and Yoshikawa, S. (2001) *Acta Crystallogr. Sect. D Biol. Crystallogr.* **57,** 941–947

28. Wittig, I., Carrozzo, R., Santorelli, F. M., and Schägger, H. (2006) *Biochim. Biophys. Acta* **1757,** 1066–1072

29. Pearce, D. A., and Sherman, F. (1995) *Proc. Natl. Acad. Sci. U. S. A.* **92,** 3735–3739

30. Roberts, V. A., and Pique, M. E. (1999) *J. Biol. Chem.* **274,** 38051–38060

31. Meisinger, C., Pfanner, N., and Truscott, K. N. (2006) *Methods Mol. Biol.* **313,** 33–39

32. Schägger, H., and von Jagow, G. (1991) *Anal. Biochem.* **199,** 223–231

33. Wittig, I., Braun, H. P., and Schägger, H. (2006) *Nat. Protocols* **1,** 418–428

34. Sunderhaus, S., Eubel, H., and Braun, H. P. (2006) in *Mitochondrial Genomics and Proteomics Protocols*, *Methods in Molecular Biology Series* (Leister, D., and Herrmann, J., eds) Humana Press, Totowa, NJ, in press

35. Neuhoff, V., Arold, N., Taube, D., and Ehrhardt, W. (1988) *Electrophoresis* **9,** 255–262

36. Zerbetto, E., Vergani, L., and Dabbeni-Sala, F. (1997) *Electrophoresis* **18,** 2059–2064

37. Penczek, P., Radermacher, M., and Frank, J. (1992) *Ultramicroscopy* **40,** 33–53

38. Ludtke, S. J., Baldwin, P. R., and Chiu, W. (1999) *J. Struct. Biol.* **128,** 82–97

39. Van Heel, M., Gowen, B., Matadeen, R., Orlova, E. V., Finn, R., Pape, T., Cohen, D., Stark, H., Schmidt, R., Schatz, M., and Patwardhan, A. (2000) *Q. Rev. Biophys.* **33,** 307–369

40. Van Heel, M. (1987) *Ultramicroscopy* **21,** 95–100

41. Guex, N., and Peitsch, M. C. (1997) *Electrophoresis* **18,** 2714–2723

42. DeLano, W. L. (2002) *The PyMOL Molecular Graphics System*, DeLano Scientific, San Carlos, CA

43. Harris, J. R., and Horne, R. W. (1994) *Micron* **25,** 5–13

44. Kim, C. H., and King, T. E. (1983) *J. Biol. Chem.* **258,** 13543–13551